Check for updates

RESEARCH ARTICLE

steel research international

www.steel-research.de

Effects of Constituent Hardness on Formability of Dual Phase Steels

Mark D. Taylor,* Emmanuel De Moor, John G. Speer, and David K. Matlock

A commercially produced 0.15% carbon dual phase (DP) steel with 1081 MPa tensile strength is modified to create eight additional conditions using tempering or tempering plus cold-rolling, processes that are shown to primarily affect constituent (martensite and ferrite) hardness as measured with nanoindentation. The effects of different martensite/ferrite hardness ratios are evaluated using tensile and hole expansion testing. Lower martensite/ferrite hardness ratios (increased similarity between ferrite and martensite hardness) are interpreted to improve strain sharing, which suppresses plastic strain localization to higher stresses for yield strength and results in higher hole expansion ratios. Microstructure-level strain maps created using digital image correlation on deformed tensile samples illustrate that plastic strains heterogeneously develop, with the largest local strains residing in ferrite at interfaces with martensite, locations consistent with preferential void nucleation sites in DP steels. Metallographic assessments of the extent of void formation in the necked regions of failed tensile samples show that for a given local thickness strain, the extent of void formation is significantly less in steels with lower martensite/ferrite hardness ratios, further illustrating the importance of controlling martensite/ferrite hardness ratios to optimize forming responses of DP steels.

1. Introduction

Advanced high strength steels (AHSS) in the automotive industry have continued to replace lower strength mild steels, allowing manufacturers to reduce vehicle weight and increase fuel efficiency, all while maintaining occupant safety. Dual phase (DP) steels are a category of AHSS that are popular with automotive manufacturers, and are generally composed of a soft ferrite matrix with interspersed hard martensite islands. Relative to other AHSS grades, DP steels have a low alloying requirement, good combinations of strength and ductility, a low yield ratio, and can be processed to produce a wide range of ultimate tensile strengths (600–1200 MPa UTS).[1–3] Furthermore, increased performance demands by industry have led to the development and production of subcategories of DP steels with specific mechanical attributes, such as increased yield ratio, stretch flangeability, or bendability.[4] However, higher strength DP steels (UTS of 780 MPa and greater) have exhibited fracture during forming operations at limits below values expected using traditional prediction methods, such as forming limit diagrams and total elongations (TE) obtained from uniaxial tensile tests.[5–10] These unpredictable, localized fractures in higher strength DP steels are one challenge to the automotive industry. Tensile elongation derives from global fracture, where deformation mechanisms on the scale of the entire specimen are active.[11] In contrast, industrial forming operations can promote localized fracture, where fracture mechanisms on the order of several grains can dictate performance.[12]

Laboratory tests such as stretch bending and hole expansion testing have been used to evaluate local formability characteristics in higher strength DP steels.[13–15] Both stretch bending and hole expansion tests induce triaxial stresses and are interpreted to be representative of some industrial forming modes.[6,9] Hole expansion tests are designed to evaluate fracture-sensitive microstructures by imposing deformation histories simulating those experienced at unconstrained sheet edges present at sheared holes, edges, and so on, during industrial sheet forming operations.[16] Test sample results are expressed as hole expansion ratios (HERs), i.e., the percent increase in diameter until the onset of edge cracking in a round hole in the center of a laboratory sample forced to expand on a specialized test system.[13] While the hole in hole expansion test specimens can be created by drilling, electric discharge machining, and shearing, sheared holes are of most interest because shearing is typically used to prepare blanks for industrial stamping operations.[16–18] The shearing process induces a region of shear deformation adjacent to the hole edge and local nonuniform geometry with the presence of a burr, both of which enhance local cracking in the region of the hole.[19,20] Due to the two-phase microstructure in DP steels, the triaxial stress state created during hole expansion testing has been observed to accelerate strain localization into ferrite, making ferrite a "weak link."[7,19,21] These heterogeneous strain distributions within the microstructure facilitate void nucleation and growth at lower macroscopic strains than would be expected if strains were uniformly distributed throughout the microstructure.[22] Multiple studies incorporating hole expansion testing of DP steels have concluded that HER improved with a decrease in the relative hardness between

M. D. Taylor, E. De Moor, J. G. Speer, D. K. Matlock
Advanced Steel Processing and Products Research Center
Colorado School of Mines
1500 Illinois Street, Golden, CO 80401, USA
E-mail: mark_taylor_06@hotmail.com

The ORCID identification number(s) for the author(s) of this article can be found under https://doi.org/10.1002/srin.202100281.

DOI: 10.1002/srin.202100281

martensite and ferrite.[2,7,23–26] With a decreasing martensite/ferrite hardness ratio, the "weak link" becomes stronger and/or the martensite becomes softer, enabling the microstructure to experience more homogeneous plastic deformation and delay strain localization.[8] Tempering of DP steels to preferentially decrease the hardness of martensite has been shown to be one effective way to alter the constituent hardness ratio.[17,25]

Void formation in DP steels primarily occurs at ferrite/martensite interfaces, though voids have also been observed at ferrite/ferrite boundaries, ferrite/inclusion boundaries, and even due to fracture of martensite islands.[27–29] During plastic deformation of DP steels, the soft ferrite primarily accommodates strain, while the harder martensite islands primarily accommodate stress, creating regions of interfacial strain heterogeneity and incompatibility, leading to void formation.[21,30–33] **Figure 1** shows a scanning electron microscope (SEM) micrograph of a 0.15 wt % carbon DP980 steel (DP steel with a minimum 980 MPa UTS) that exhibits voids, highlighted by arrows, at ferrite/martensite interfaces in a sample deformed in tension to failure.[34] In Figure 1, the lighter-colored constituent is martensite (labeled "M"), the darker-colored constituent is ferrite (labeled "F"), and the voids appear black (white arrows).

Damage accumulation in the form of voids during plastic deformation of DP steels has been characterized with multiple techniques including metallography and X-ray tomography (XRT).[11,12,34–37] Using a 0.08 wt% carbon DP600 steel, Landron et al. utilized XRT to evaluate round (smooth) and notched tensile specimens and showed the void population to exponentially increase with strain for both specimens.[12] However, the rate of void nucleation was greater for the notched specimen where the notch induced a local, triaxial stress state during deformation, leading to enhanced void nucleation at lower local strains.[11,21,32,37] The extent of strain partitioning between ferrite and martensite leading to void nucleation and growth in DP steels has been the subject of multiple investigations, with the magnitude of strain partitioning dependent on the hardness ratio of martensite to ferrite and the size and distribution of martensite islands within the microstructure.[27,38–40] In general, for DP steels of a given strength, void nucleation is enhanced with an increase in the martensite/ferrite hardness ratio or an increase in the mean-free-path between martensite islands leading to greater strain heterogeneity and void nucleation at ferrite/martensite interfaces.[40–45]

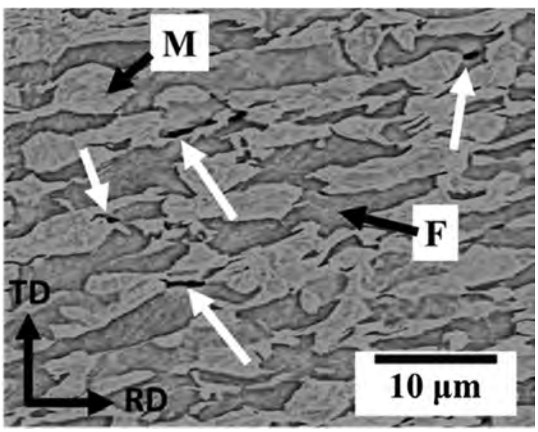

Figure 1. SEM micrograph of a 0.15 wt% carbon DP980 steel deformed in tension exhibiting ferrite/martensite decohesion at multiple locations (indicated with white arrows). Martensite is the lighter-colored constituent (labeled "M"), ferrite is the darker-colored constituent (labeled "F"), and voids are black. Tensile axis is horizontal, and the steel was etched with 2% nital.[34]

Recently, nanoindentation techniques have been used to directly quantify the hardness of individual constituents in DP steels as well as characterizing hardness gradients which evolve during deformation within individual grains.[18,25,46–50] In addition, digital image correlation (DIC) techniques applied to SEM images of deformed microstructures have been used to characterize the microscale evolution of localized strain gradients that develop during deformation of DP steels.[29] DIC results have confirmed that strain localization occurs at ferrite/martensite interfaces, with the severity increasing with greater hardness difference between ferrite and martensite.[40,51]

Past studies on formability of higher strength DP steels (780 MPa UTS and greater) typically utilized multiple materials, all with differing microstructural properties (grain size, martensite volume fraction [MVF], morphology, chemistry, and constituent hardness).[13–15] However, in DP steels, the individual microstructural properties (MVF, constituent hardness, grain size, chemistry, morphology, etc.) contribute interactively to the subsequent formability, and attempting to modify one property usually has an influence on others, making a conclusive statement about the effect of any single property challenging.[7,30] Thus, the purpose of the present study was to utilize a single DP steel with a fixed starting chemistry and microstructure (i.e., MVF, martensite distribution, and constituent grain size), and then through unique processing histories isolate the effects of constituent hardness on subsequent formability performance as assessed with hole expansion ratios. Specific variations in constituent properties, as measured by nanoindentation testing, were achieved via cold-rolling and tempering.

2. Experimental Section

2.1. Material

An uncoated 1 mm-thick DP980 steel with composition shown in **Table 1** was selected for analysis. The commercially produced steel was provided after experiencing a proprietary continuous annealing processing history. Systematic modifications to the constituent properties of the as-received DP980 steel (referred to as AR) were achieved by tempering or tempering plus cold-rolling. Four tempered conditions with UTS targets of 1050, 1020, 990, and 960 MPa were produced for tensile and hole expansion test specimens using different combinations of tempering time and temperature. Strength targets were separated by 30 MPa to reduce the potential for overlapping UTS values after tempering, and 960 MPa UTS was the lowest strength pursued

Table 1. Chemical composition [wt%] for the DP980 steel.

[wt%]	C	Mn	P	S	Si	Al	Nb	Ti	N
DP980	0.15	1.46	0.010	0.007	0.3	0.04	<0.003	0.002	0.004

Table 2. Tempering (time and temperature) and cold-rolling parameters used for the four tempered (AT) and four temper plus cold rolled (TCR) conditions.

Condition	Temper temperature [°C]	Temper time [min]	%CR [%]
AR			
1050AT	175	162	
1020AT	200	156	
990AT	250	126	
960AT	275	265	
1050TCR	175	162	1.2
1020TCR	200	156	5.5
990TCR	250	126	12.6
960TCR	275	265	20.4

so the project would remain relevant to higher strength DP steels. In DP steels, it has been shown that tempering primarily softens the martensite phase, thereby modifying constituent hardnesses without appreciably affecting other microstructural characteristics (i.e., grain size, MVF, morphology).[25,45,52,53] Tempering was performed in open atmosphere furnaces at temperatures between 175 and 275 °C for times up to 265 min. The specific combinations of tempering times and temperatures, and the corresponding condition designations for the four as-tempered (AT) conditions are shown in **Table 2**. Procedures used to identify these parameters are summarized elsewhere.[34] For each condition designation, the number corresponds to the target UTS value in the AT condition.

Processing by tempering plus cold-rolling produced four additional conditions, all with UTS values equivalent to the AR condition, but with variations in yield strength (YS), tensile elongation, and constituent hardness. Cold-rolling along the original rolling direction was performed at room temperature on both tensile and hole expansion test specimens that were tempered using time—temperature combinations equivalent to the four AT conditions in Table 2. All samples were lubricated prior to rolling; tensile samples were rolled on a two-high mill with 92 mm diameter work rolls and hole expansion coupons were rolled on a mill with 610 mm diameter work rolls. For hole expansion coupons, the percent cold reduction (%CR) was evaluated at mid-width to obtain more accurate measurements in the region where the sheared hole would be located. The %CR along with the prior tempering parameters for the four temper plus cold roll (TCR) conditions are also shown in Table 2. To achieve the desired set of samples with nearly identical UTS values, Table 2 shows that the required %CR increased with the extent of tempering. Identification of the required tempering parameters and %CR values for each AT and TCR condition reported in Table 2 involved a systematic iterative process discussed in detail elsewhere.[34]

Figure 2a shows an SEM micrograph of the AR DP980 steel oriented to view the rolling plane. In Figure 2a, the steel was ground and polished to 1 μm using standard metallographic techniques and then etched with 2% nital for ≈10 s to reveal the microstructure. The darker, featureless regions are interpreted to be ferrite (labeled "F" in Figure 2a), and the brighter regions with distinct interior etching response, sometimes accompanied by a white outline, are interpreted to be martensite (labeled "M").

2.2. Microstructural Characterization Techniques

2.2.1. Grain Size and MVF

Select conditions from Table 2 were characterized with a two-phase grain size/MVF measurement technique adapted from Higginson and Sellars.[54] For each condition, the rolling plane and longitudinal plane (defined by the rolling direction and sheet normal) cross sections were mounted and polished to 1 μm diamond using standard metallographic techniques and etched with 2% nital for ≈10 s. Six SEM micrographs were acquired for each orientation, totaling 12 micrographs per condition. Each micrograph was analyzed twice by randomly locating an overlay containing three concentric circles with 60 proportionally spaced tick marks. For each measurement field, the 60 tick marks were used to determine MVF using standard point counting methods, and circumference intercepts with ferrite/ferrite and ferrite/martensite boundaries were separately counted to determine average grain sizes for both constituents.

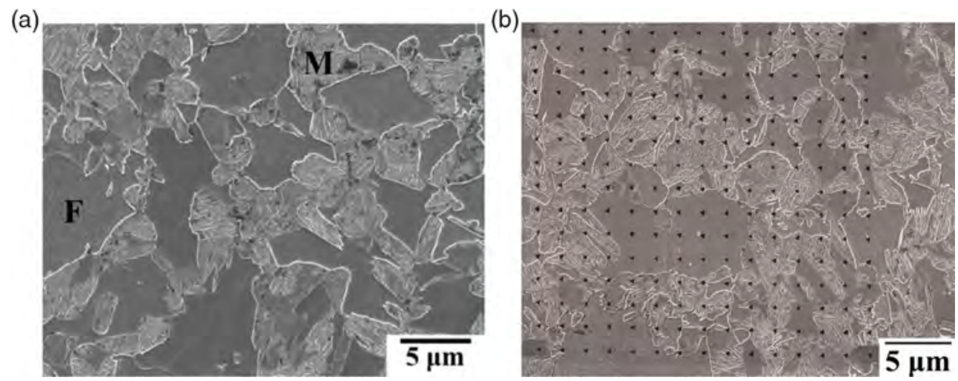

Figure 2. a) SEM micrograph of the rolling plane orientation of the commercially produced DP980 steel in the AR condition. The lighter-colored constituent is martensite (labeled "M"), and the darker-colored constituent is ferrite (labeled "F"). b) SEM micrograph of the 1020AT condition with a 15 × 15 indent array overlaid, allowing the determination of each indent location with respect to the phase(s) present. 2% nital etch.

2.2.2. Retained Austenite Content

The retained austenite content of the AR DP980 steel was determined from X-ray diffraction (XRD) data. Specimens oriented to view the rolling plane for XRD analysis were mechanically polished to 6 μm using standard metallographic techniques, and then submerged for 5 min in a solution of hydrofluoric acid, hydrogen peroxide, and deionized water to remove any potential surface effects due to mechanical polishing (e.g., mechanically induced transformation of austenite to martensite, if present).

2.2.3. Nanoindentation Hardness Testing

Nanoindentation was used to quantify the average ferrite and martensite hardness values for the AR and eight modified conditions (four AT, four TCR in Table 2). Metallographic samples for nanoindentation analysis were mounted to view the rolling plane, polished to 1 μm using standard metallographic techniques, and finished by vibratory polishing for 10 h with 0.05 μm colloidal silica. Vibratory polishing with colloidal silica is both a mechanical and chemical material removal method, and is interpreted to remove much of the surface-hardened layer induced by the mechanical polishing steps.[55] A nanoindenter equipped with a Berkovich indenter tip was used to perform a 15 × 15 array (225 total) of indents spaced 2 μm apart to a depth of 40 nm using a 2 s load–2 s hold–2 s unload function on the as-polished surface for each condition in Table 2. Prior to indentation, a tip area function was performed on fused silica for the Berkovich tip, and hardness values were shown to be accurate to depths as low as 25 nm. All indents in this study were performed in displacement control to a depth of 40 nm to circumvent the additional variation caused by indentation size effect, where shallower indentation depths exhibit higher hardness values compared with deeper indentation depths in the same material.[49] A Berkovich indenter was selected as it has been shown that the induced deformation field is resistant to material pileup and can also generate sufficient plastic zones at shallow indentation depths (<30 nm).[56] Figure 2b shows an SEM micrograph of the 1020AT condition with the 15 × 15 nanoindentation array as viewed on a polished steel surface overlaid on the image of the etched sample surface. The load—displacement curves generated from the indents were used to calculate hardness with the Oliver—Pharr method.[57] Average ferrite and martensite constituent hardness values were obtained for each condition by categorizing the 225 indents using a method outlined elsewhere.[58] Indents located within 1.5 indent diameters of a boundary were discarded from analysis due to potential effects of neighboring constituents or to strengthening effects from the adjacent phase/boundary, and all other indents located entirely within either ferrite or martensite were used to determine the average ferrite and martensite hardness, respectively.[47]

2.3. Tensile Testing

Uniaxial tensile testing was performed using ASTM E8 standard size tensile specimens with a reduced gauge section of 57 mm × 12.7 mm × sheet thickness. Three tensile tests were performed for the AR and eight modified conditions. All tensile tests were performed with the tensile axis parallel to the rolling direction, strain was monitored using a 51 mm extensometer, and all tests imposed an engineering strain rate of 0.0025 s^{-1}. For each tensile test, data were plotted as engineering stress versus engineering strain and the YS, UTS, uniform elongation (UE), and TE were determined using standard procedures. In the event of continuous yielding, a 0.2% strain offset was used to quantify YS, and in the event of discontinuous yielding, the lower yield point was used. Selected tensile tests for DIC analyses discussed below were performed on ASTM E8 subsized tensile specimens with a reduced gauge section of 32 mm × 6.4 mm × sheet thickness. Tests were performed with the tensile axis parallel to the rolling direction at the same imposed strain rate used for the standard sized specimens and strain was monitored using a 25.4 mm gauge length extensometer.

2.4. Hole Expansion Testing

Hole expansion tests were performed on the AR and eight modified conditions using square coupons, approximately 100 × 100 mm, prepared with a 10 mm diameter sheared hole in the center of each test coupon. The holes were sheared with a die/punch clearance of 10—12.5%, in accordance with ISO 16630. For the AT and TCR conditions, tempering or tempering plus cold-rolling were performed prior to hole punching. An unlubricated, 60° conical punch traveling uniaxially at 20 mm min^{-1} was used for hole expansion tests. Coupons were tested with the sheared burr oriented away from the punch contact surface (burr-up position). The conical punch and the 10 mm sheared hole were concentric throughout the test. A clamping force of 22 kN was used to prevent the coupons from drawing upward during the test. A high-speed camera positioned such that the 10 mm sheared hole was centered in the image frame was used for image acquisition during testing. Failure was defined as the development of a through-thickness crack exceeding 0.1 mm in width, and the HER (expressed as %) was determined using Equation (1), where d_o and d_f are the initial and final hole diameters, respectively.

$$\mathrm{HER}\,[\%] = \frac{(d_f - d_o)}{d_o} \times 100 \quad (1)$$

The initial and final hole diameters were measured using the images acquired during testing with ImageJ, an open platform scientific image processing program. The initial hole diameter was measured using an image prior to the conical punch travel, and the final hole diameter was measured on the first in situ image that identified a 0.1 mm through-thickness crack. **Figure 3** shows an example image of an in situ hole expansion test at failure for the AR condition. Diameter measurements were taken along four reference lines (identified as M1 to M4) at 45° angles, and both the initial and final diameters used in the HER calculations represent the average of these four measurements. Between three and five hole expansion tests were performed for each condition, as shown in Table 2.

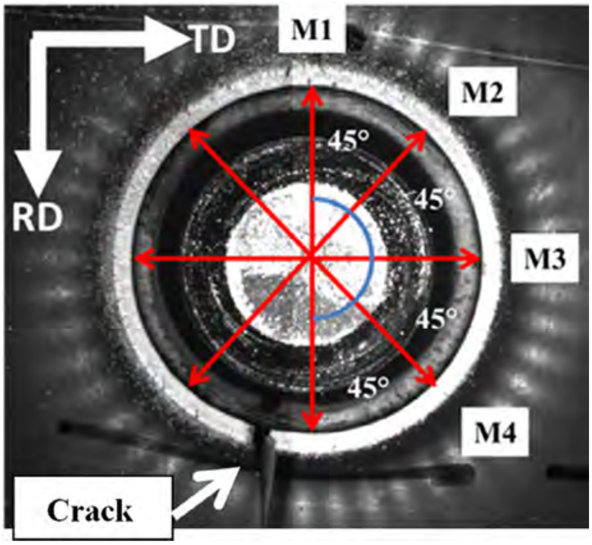

Figure 3. Image of a hole expansion test on the AR condition (after failure) illustrating the four measurement locations (M1–M4). The bright ring is the sheared hole surface, and a crack is located at the bottom of the sheared hole. The bright circle in the center is the top of the 60° conical punch. The bright features surrounding the sheared hole are from an LED light ring used for illumination during image acquisition.

2.5. Digital Image Correlation Methods

Strain partitioning between ferrite and martensite during deformation was directly evaluated using DIC methods applied to specially prepared deformed tensile specimens of the AR and 960TCR conditions. Prior to deformation, the reduced tensile gauge sections on ASTM E8 subsized tensile specimens were polished to 1 μm using standard metallographic techniques and etched with 2% nital for approximately ≈8 s. For each condition, selected areas in the sheet rolling plane within the gauge section were evaluated using DIC. Ten SEM images of the initial (undeformed) state were acquired from each selected area to assess the magnitude of drift during image acquisition as beam drift during SEM image acquisition can create artificial strains.[40,59] For all SEM images used for DIC, equivalent acquisition parameters (magnification, working distance, resolution, etc.) were used. After imaging the initial undeformed state, the E8 subsized tensile specimens were removed from the SEM, deformed to a predetermined uniaxial strain, unloaded, and placed back into the SEM chamber to image the same area. Ten SEM images of the deformed state were also acquired to assess beam drift. The SEM images were evaluated using NCORR, an open-source 2D DIC analysis software.[60] For all DIC calculations, a 15-pixel radius subset size and a 2-pixel subset spacing were used. After the background strains associated with beam drift at each state were established, images from different states (undeformed and deformed) were analyzed with DIC to characterize the distribution of strains within the microstructure. The results are presented as strain maps over areas sufficiently large (≈30 μm × 30 μm) to encompass multiple regions of each constituent. A more detailed explanation of the DIC methodology can be found elsewhere.[34]

2.6. Quantitative Assessment of Strain-Dependent Void Formation

The void area % as a function of thickness strain for the AR, 960AT, and 960TCR conditions was characterized using fractured ASTM E8 standard size tensile specimens. For each condition, the fractured end of the tensile specimen was sectioned through-thickness at mid-width to view the longitudinal plane (i.e., the plane defined by the rolling direction and sheet normal), mounted and polished to 1 μm using standard metallographic techniques, and etched with 2% nital for ≈8 s. Nine defined steps from the fracture surface were established, and five SEM micrographs proportionally spaced along the thickness direction were acquired at each of the nine steps. All SEM images for the void analysis study were taken using equivalent image acquisition parameters. **Figure 4** shows an SEM micrograph of a fractured ASTM E8 standard size tensile specimen for the 960TCR condition in the longitudinal orientation, and illustrates the location of the five SEM images (black boxes) for the first eight steps. In Figure 4, the fracture end is on the left side, the thickness direction is vertical, and the dashed white line, parallel to the sheet rolling direction, indicates midthickness.

The SEM images acquired at each of the nine steps were analyzed for void area % with ImageJ using a grayscale threshold to discriminate between voids (black) and the steel substrate (white). Thickness strains for each of the nine steps were calculated using Equation (2) where t_{local} is the local thickness (in mm) measured on the micrographs, and t_{i} is the initial thickness of the tensile specimen (in mm).

$$\text{Local Thickness Strain}\,[\%] = \frac{(t_{\mathrm{i}} - t_{\mathrm{local}})}{t_{\mathrm{i}}} \times 100 \tag{2}$$

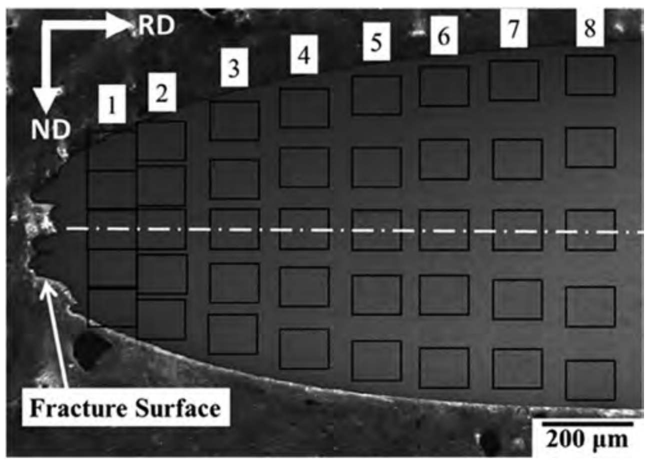

Figure 4. SEM micrograph showing the longitudinal orientation of the fractured end of a 960TCR condition ASTM E8 tensile specimen. Black boxes represent approximate locations where SEM micrographs were acquired for void analysis for the first eight steps. Fracture surface is on the left-hand side of the image, and thickness direction is vertical. The white dashed line represents the midthickness of the tensile specimen.

3. Results

3.1. Microstructural Characterization

Based on quantitative metallography, the AR condition exhibited an average ferrite grain size of 2.9 μm, a mean martensite island size of 3.1 μm, and an MVF of 54.5%. However, as the MVF exceeded the percolation limit (about 29.5%), the probability of independent martensite grains sharing an interface increased, potentially leading to a less accurate calculation of mean martensite island size. Thus, an alternate approach, based on the empirical analysis discussed by Scott *et al.* which utilizes ferrite grain size and MVF as inputs, was also used and the calculation resulted in a mean martensite island size of 3.2 μm, i.e., essentially equivalent to the initial quantitative metallography results.[25] The 960TCR condition was also evaluated because it experienced the greatest degree of tempering and the highest %CR. Only minor differences in average ferrite grain size, mean martensite island size, and MVF were observed, and the values were interpreted to be within the experimental uncertainty of the technique. Based on the similarities in average grain size and MVF for the AR and 960TCR conditions, it was interpreted that microstructural properties of grain size and MVF were effectively constant for all nine conditions reported in Table 2. The AR condition exhibited an austenite content below the XRD detection limit (≈3 vol%), and it was determined that all nine steel conditions in Table 2 had austenite contents below 3 vol% because tempering and cold-rolling operations act to further reduce austenite in DP steels.

3.2. Tensile and Hole Expansion Properties

The multiple tensile tests for all material processing conditions exhibited excellent reproducibility and **Figure 5**a shows representative engineering stress-engineering strain tensile curves for the AR and four AT conditions. The tensile curves in Figure 5a illustrate that with an increase in the extent of tempering, the UTS systematically decreased consistent with the experimental design outlined earlier. The AR condition exhibited continuous yielding behavior characteristic of many DP steels, while all four tempered (AT) conditions exhibited yield point elongation (YPE), the magnitude of which increased with aging temperature. Associated with the transition from continuous to discontinuous yielding with aging, the YS increased and correspondingly the uniform and total ductility decreased.

Table 3. Average tensile properties and HER for the nine steel conditions. Tensile data represent the average of three independent tests and HER values average three to five tests per condition. Standard deviations for each entry are shown in italics in parentheses next to the average values.

Condition	YS [MPa]	UTS [MPa]	UE [%]	TE [%]	HER [%]
AR	627 *(15.1)*	1081 *(7.9)*	7.8 *(0.4)*	11.7 *(0.2)*	29.3 *(1.6)*
1050AT	651 *(18.6)*	1052 *(11.8)*	7.7 *(0.5)*	11.7 *(0.7)*	30.2 *(0.9)*
1020AT	725 *(32.1)*	1029 *(5.9)*	6.9 *(0.3)*	11 *(1.0)*	31.8 *(3.4)*
990AT	780 *(15.5)*	984 *(11.3)*	6.4 *(0.4)*	11.1 *(0.3)*	38.4 *(3.8)*
960AT	809 *(8.1)*	954 *(6.8)*	5.6 *(0.1)*	10.1 *(0.3)*	43.2 *(2.4)*
1050TCR	884 *(34)*	1083 *(19)*	5.6 *(0.4)*	9.8 *(1.1)*	31.8 *(3.2)*
1020TCR	979 *(14)*	1090 *(5)*	2.3 *(0.2)*	6.1 *(0.7)*	37.2 *(2.2)*
990TCR	1003 *(16)*	1083 *(10)*	1.3 *(0.2)*	3.9 *(0.4)*	39.4 *(5.0)*
960TCR	1007 *(14)*	1080 *(5)*	1.2 *(0.1)*	3.6 *(0.1)*	39.3 *(3.3)*

Figure 5b shows representative engineering stress-engineering strain tensile curves for the AR and the four temper plus cold-roll (TCR) conditions. All four TCR conditions (1050TCR, 1020TCR, 990TCR, and 960TCR) achieved UTS values equal to the AR condition and exhibited continuous yielding consistent with normally observed behavior for cold rolled steels. As shown in Table 2, the extent of cold-rolling required to increase the UTS of the tempered conditions so that the values would coincide with the AR UTS material increased with a decrease in UTS after tempering. As a result of cold work, the total elongations of the TCR samples decreased, with the 960TCR sample in Figure 5b having the lowest UTS after tempering and requiring the greatest amount of cold-rolling (20.4% reduction in thickness) to increase the UTS to the desired value.

Table 3 shows the tensile properties for the AR and eight modified conditions and includes YS, UTS, UE (taken as the plastic

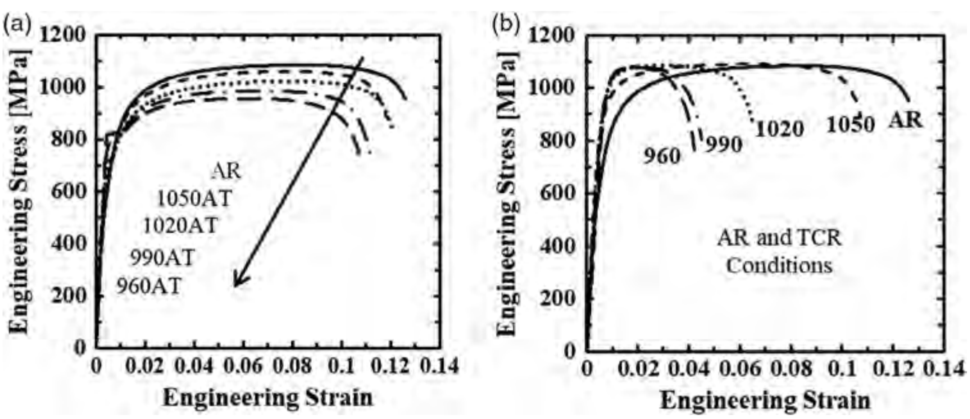

Figure 5. a) Representative engineering stress-engineering strain tensile curves for 1050AT, 1020AT, 990AT, 960AT, and the AR conditions, and b) engineering stress-engineering strain tensile curves for 1050TCR, 1020TCR, 990TCR, 960TCR, and AR conditions.

Table 4. Nanoindentation average ferrite (α) hardness, average martensite (α') hardness, and the martensite/ferrite (α'/α) hardness ratio for the nine conditions of DP980. Standard deviations for the individual constituent properties are shown in italics in parentheses next to the average values.

Condition	α [GPa]		α' [GPa]		α'/α
AR	2.15	*(0.42)*	6.84	*(0.96)*	3.18
1050AT	2.2	*(0.33)*	6.2	*(0.68)*	2.82
1020AT	2.25	*(0.50)*	6.05	*(0.81)*	2.69
990AT	2.05	*(0.28)*	5.27	*(0.86)*	2.57
960AT	1.93	*(0.28)*	5.18	*(0.85)*	2.68
1050TCR	2.45	*(0.33)*	6.21	*(0.74)*	2.54
1020TCR	2.18	*(0.27)*	5.53	*(0.69)*	2.54
990TCR	2.28	*(0.38)*	5.34	*(0.74)*	2.34
960TCR	2.25	*(0.38)*	5.08	*(0.78)*	2.26

strain at peak load), and TE for each steel. Table 3 shows the average properties from three tensile tests per condition and the corresponding standard deviations for each reported value. The AR condition exhibited a UTS of 1081 MPa, while the four AT conditions each exhibited UTS values close to their respective target (e.g., the 1050AT condition exhibited an average UTS of 1052 MPa). The decrease in TE with increasing tempering temperature for the AT conditions is consistent with observations from other studies on tempering of DP steels.[61,62] For the TCR conditions, an increase in %CR corresponded to a decrease in TE and increase in YS. The experimental results shown in Figure 5 and Table 3 confirm that the basic experimental premise on which this study is based, i.e., achieving systematic variations in mechanical properties in a DP steel with a constant composition, MVF, martensite size and distribution, and ferrite grain size, was achieved. Thus, it is interpreted that the observed variations in mechanical properties primarily reflect variations in constituent hardness.

Hole expansion tests were performed to evaluate local formability performance for the AR and eight modified conditions, and average HER values, based on three to five tests per condition, are shown in Table 3. Also included are calculated standard deviations for each reported HER average. All eight modified conditions exhibited HER values greater than the AR condition. For the AT conditions, HER values increased with higher tempering temperature, and for the TCR conditions, HER values increased with %CR. In every case, the 0.1 mm through-thickness crack (failure criteria) developed along the rolling direction.

3.3. Constituent Hardness

Nanoindentation was performed on the AR and eight modified conditions, and **Table 4** shows the average ferrite hardness, average martensite hardness, and martensite/ferrite hardness ratio for each condition. Also included in Table 4 are standard deviations for each reported average. The range of ferrite and martensite hardness values reported in Table 4 is consistent with results reported in the literature.[50,63–65] The AR and eight modified conditions all exhibited similar hardness distributions for ferrite and martensite, and **Figure 6**a,b shows representative hardness histograms for the ferrite hardness data and martensite hardness data, respectively, for the AR condition. For all nine conditions, ferrite hardness data exhibited essentially a normal distribution, with typical ferrite hardness values ranging between 1.7 and 3.5 GPa. Though the ferrite hardness distribution in Figure 6a is similar to previously reported nanoindentation data on DP steels, the average ferrite hardness values reported in Table 4 are lower than those observed for several DP980 steels investigated in a previous study utilizing the same nanoindentation methodology.[18] The lower ferrite hardnesses reported in Table 4 are attributed to the fact that the current steel was produced from a leaner alloy with lower amounts of solid solution strengthening elements (e.g., Si and Mn) and without microalloy additions which may have contributed to precipitation strengthening of ferrite in the previous study.[18] The martensite hardness distributions for the AR and eight modified conditions were skewed slightly toward the lower portion of the hardness range, and can be seen in Figure 6b. The observation of a skewed hardness distribution for martensite has also been reported previously and attributed to potential alloy content variations within the martensite.[18,25]

The nanoindentation hardness data in Table 4 quantitatively illustrate the effects of the different processing pathways on the constituent hardness values. Compared with the AR condition, the tempered (AT) conditions exhibited a more appreciable

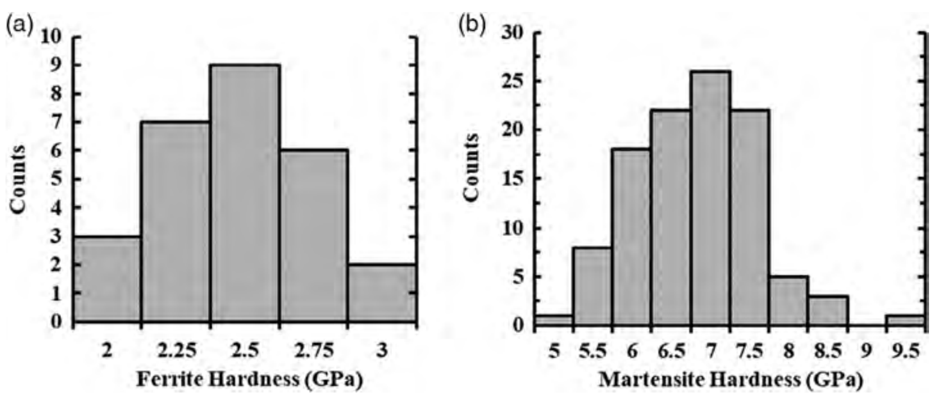

Figure 6. Hardness histograms of a) ferrite and b) martensite for the AR condition.

decrease in martensite hardness (from 6.20 for AR to 5.18 GPa for 960AT) than in ferrite hardness (2.20—1.93 GPa), indicating that tempering primarily softens martensite in DP steels. After cold-rolling, Table 4 shows that TCR conditions experience a more appreciable increase in ferrite hardness relative to martensite hardness, indicating that cold-rolling primarily work-hardened ferrite. Both tempering and cold-rolling treatments acted to reduce the martensite/ferrite hardness ratio, creating a range of hardness ratios for subsequent analyses. As reported elsewhere, nanoindentation hardness testing was also used to evaluate the effects of work hardening in the heavily deformed shear zone adjacent to the punched hole in the hole expansion test samples discussed in Section 2.4.[34] The intense local shear deformation was shown to work harden both ferrite and martensite, but the extent of the work hardening in ferrite was greater, leading to a localized decrease in the martensite/ferrite hardness ratio in the region adjacent to the sheared hole.

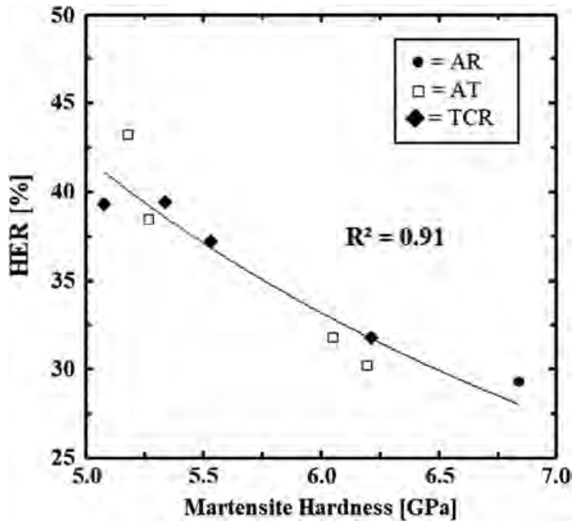

Figure 8. HER plotted as a function of martensite hardness for the AR and eight modified conditions.

3.4. Correlations between Constituent Hardness and Mechanical Properties

The martensite/ferrite hardness ratio was chosen to establish correlations with HER and tensile properties because it incorporates the hardness from both ferrite and martensite and was interpreted to best represent the unique hardness state of each steel condition in this study. **Figure 7**a correlates HER with the martensite/ferrite hardness ratio, and shows that for the AT and TCR conditions, HER increases with a decrease in hardness ratio, and that both sets of data reasonably fit a single function that also includes the AR condition.

The trend observed in Figure 7a is also consistent with previously reported data, and quantitatively indicates that microstructural modifications which decrease the hardness differences between constituents (i.e., lower hardness ratio) correspond to improved performance in complex forming operations, even for steels of equivalent UTS.[7,8,18,21,27,58] A lower hardness ratio is interpreted to increase strain-sharing between ferrite and martensite during deformation, allowing the microstructure to delay strain localization in ferrite to higher formability limits. One potential outlier in Figure 7a is the 960AT condition (HER = 43.2 and hardness ratio = 2.68). Based on the standard deviations reported for ferrite and martensite hardness in Table 4, the modest reduction in constituent hardness for the 960AT condition might reflect the statistical nature associated with nanoindentation, and further testing may be required. Note that for Figure 7a and all subsequent correlation plots, the solid circle represents the AR condition, the solid diamonds represent the TCR conditions, and the open squares represent the AT conditions.

Figure 7b shows an increase in YS with decreasing hardness ratio for the nine steel conditions. The lower hardness ratio is interpreted again to increase strain-sharing between ferrite and martensite, thereby suppressing macroscopic plastic strain to higher stresses. When considering the steel conditions of equivalent UTS in Figure 7b (filled shapes), the increase in YS with lower hardness ratio signifies that less work hardening occurred.

Figure 8 correlates HER with average martensite hardness and shows that HER increases with a decrease in martensite hardness, and the trend is similar to the correlation shown in Figure 7a for hardness ratio, i.e., HER increases with a decrease in hardness ratio. The correlation shown in Figure 8 was created

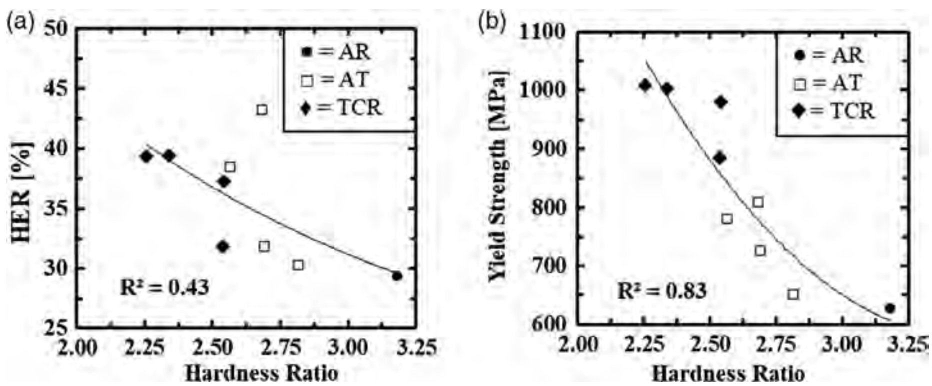

Figure 7. a) HER plotted as a function of martensite/ferrite hardness ratio for all nine conditions and b) YS plotted as a function of martensite/ferrite hardness ratio for all nine conditions.

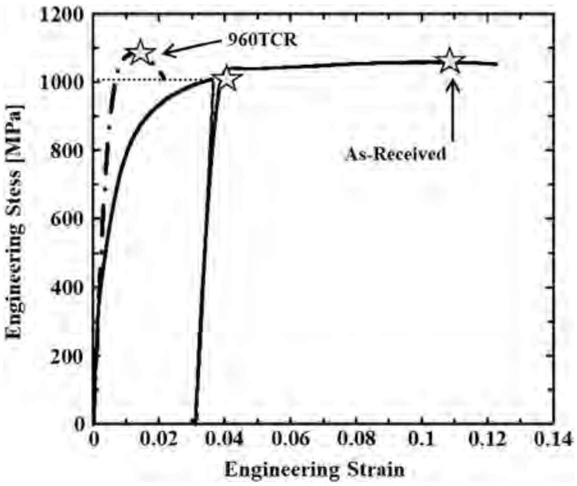

Figure 9. Engineering stress-engineering strain tensile curves for the AR (solid line) and 960TCR (dashed-dot line) conditions generated using ASTM E8 subsized tensile specimens. The stars (three total) represent the approximate locations where DIC analyses were conducted. The unloading and reloading curve associated with removal of the AR specimen for DIC analysis after a strain of about 0.03 is also shown.

using the nine steel conditions with approximately constant microstructural properties (grain size, morphology, MVF, chemistry), and has a significantly improved correlation coefficient ($R^2 = 0.91$) compared with previous results published involving eight commercially produced DP980 steels with different microstructural properties.[18] Specifically, the eight commercial steels had MVF values between 26% and 36%, i.e., levels significantly less than the 54.5% in the steel considered here indicating that to achieve DP980 properties the alloying contents and processing histories differed among the steels used, and differed from the steel used here. As a result of variations in microstructure, the observed correlation with martensite hardness exhibited a lower correlation coefficient ($R^2 = 0.54$) in the referenced study. The strong correlation shown in Figure 8 suggests that martensite hardness may be a dominant factor in achieving improved HER values.[25] Similarly, the eight commercial DP980 steels evaluated previously exhibited higher martensite hardness values (6.8—9.3 GPa) and correspondingly lower HER values (14—25%), further corroborating the importance of martensite hardness in HER performance.[18]

3.5. Microstructural Damage Analysis

The strain-mapping technique of DIC was performed on ASTM E8 subsized tensile specimens in the AR and 960TCR conditions to evaluate constituent hardness effects on the development of strain partitioning during plastic deformation. The AR and 960TCR conditions were selected as they exhibited equivalent UTS values and significant differences in other properties, including TE (11.7% and 4.0%, respectively), HER (29% and 39%, respectively), and martensite/ferrite hardness ratio (3.2 and 2.3, respectively). **Figure 9** shows the engineering stress-engineering strain curves for the two conditions, with the AR shown by a solid line and the 960TCR by a dashed-dot line. The star symbols in the image approximate the strains corresponding to the DIC analyses. Both materials were evaluated at uniform strain (UTS); 11.7% for the AR condition and 0.8% for the 960TCR condition. The AR condition was also evaluated after a strain of about 3.0% (corresponding to a stress of 1009 MPa).

Figure 10 and **11** show the resulting DIC strain maps for the three conditions identified in Figure 9. In each figure, the tensile axis is horizontal, and mapped strains represent ε_{xx}, i.e., strains in the tensile direction. The SEM micrographs are shown with the DIC strain map overlaid to provide a spatial reference for the strain gradients that developed; the ferrite appears darker-colored, and the martensite appears brighter, sometimes accompanied by a white outline. Each DIC map also includes a color scale for strain, referenced to the specific image. (Note that the relationship between color and strain level differs between each strain map presented in Figure 10 and 11). For each strain map, the average ε_{xx} strain, reported in %, for the entire area evaluated by the DIC software is shown in the bottom left corner. Note that these values reflect the effects of sampling location and differ slightly from the macroscopic strains indicated on the engineering stress-engineering strain curves in Figure 9.

Figure 10a shows a DIC strain map overlaying the microstructure of the AR condition after being strained to a flow stress of

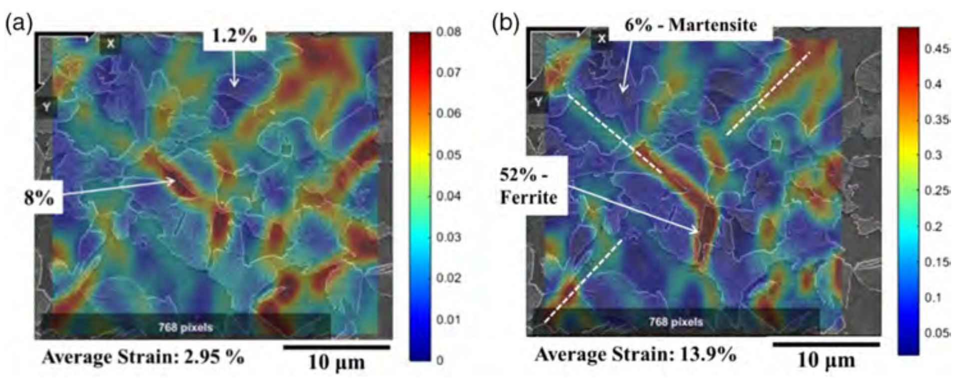

Figure 10. a) Tensile strain map for the AR condition after reaching 1009 MPa, showing diffuse regions of strain localization in regions of ferrite in proximity to martensite. b) Tensile strain map for the AR condition after being strained to the UTS (11.7% uniform strain), showing locally developed bands of strain localization within ferrite regions in proximity to martensite (white dashed lines). Tensile direction is horizontal.

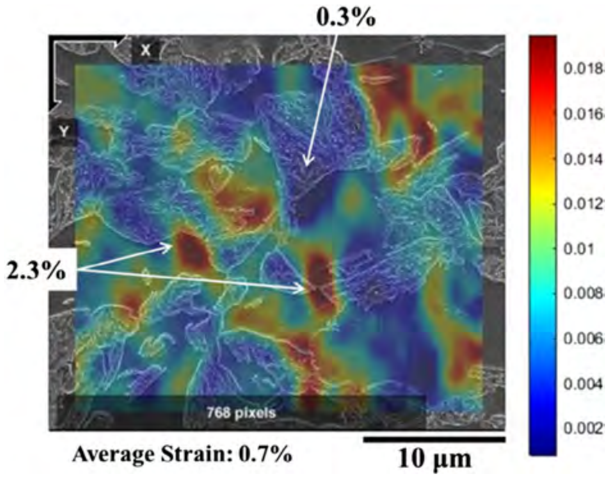

Figure 11. Tensile strain map for the 960TCR condition after being strained to the UTS, showing diffuse regions of strain localization in ferrite regions adjacent to martensite. For an average area strain of 0.7%, local strains range from 0.3% to 2.3%. Tensile direction is horizontal.

1009 MPa. This stress level was selected for analysis for the AR condition because 1009 MPa is the YS for the 960TCR condition measured at a strain of 0.2%, i.e., where little macroscopic yielding occurred. For an average strain of 2.95%, regions of the AR microstructure in Figure 10a experienced local strains ranging from 1.2% to 8%, with the highest strains located in ferrite regions adjacent to martensite (indicated as 8% in Figure 10a) and the lowest strains (1.2%) within the martensite. Locations of highest strain in Figure 10a (ferrite/martensite interfaces) coincide with the microstructural locations where voids are known to preferentially form in DP steels.[42]

Figure 10b shows a DIC strain map for the AR condition after being strained to the UTS. Compared with Figure 10a,b shows an average area strain of 13.9%, and a larger range of local strain values (6—52%) in response to increased plastic strain. In Figure 10b, lower strains reside primarily within martensite (indicated as "6%"), and higher strains in ferrite with proximity to martensite (indicated as "52%"). Areas of strain localization are similar for Figure 10a,b, and in Figure 10b, the higher local strains appear to have connected independent regions of strain localization into bands of strain localization (indicated with white dashed lines). These localized regions of higher strain in ferrite (also evident, but to a lesser degree in Figure 10a) after yielding have been observed in other studies, and are interpreted to be a primary contributor to work hardening.[21,29,40,51] As shown by a comparison of the band intensities in Figure 10a,b, the strain gradients within the developed bands increase with deformation and are believed to be preferential locations for martensite/ferrite void nucleation.

Figure 11 shows a DIC strain map of the 960TCR condition after being strained to the UTS. For an average area strain of 0.7%, local strain values ranged from 0.3% to 2.3%, indicating that strain partitioning occurs even at low plastic strains, and for low hardness ratio steels. Similar to Figure 10, regions experiencing highest local strains in Figure 11 were ferrite in close proximity to martensite (indicated as "2.3%"), and regions experiencing the lowest local strains were within martensite (indicated as "0.3%"). Compared with the AR condition in Figure 10, plastic strains are much lower in Figure 11, and appear diffuse. The development of more diffuse strains in the 960TCR specimen is interpreted to reflect the effects of martensite hardness reduction due to tempering, an observation consistent with previously reported DIC results of Kang *et al*. on a DP600 steel.[40] Thus, for the same UTS, the AR condition (Figure 10b) experienced greater heterogeneity of strain compared with the 960TCR condition (Figure 11) and supports the interpretation of Figure 7b that a lower hardness ratio allows the microstructure to suppress strain localization leading to higher observed yield strengths.[51] For all three DIC analyses (Figure 10 and 11), strain preferentially localized inside ferrite grains, with the highest strains developing in the ferrite with proximity to martensite. Upon further deformation, the localized regions of strain link to form bands of strain localization. Regardless of the martensite/ferrite hardness ratio, DIC results confirm that plastic strains heterogeneously develop in DP steel microstructures at ferrite—martensite interfaces, i.e., locations consistent with preferential void nucleation sites.

Further analysis of the importance of strain partitioning shown in the DIC images was obtained by assessing void formation in selected samples. Data were obtained from metallographic images on fractured ASTM E8 full-size tensile specimen cross sections for the AR, 960AT, and 960TCR conditions at the positions identified in Figure 4. **Figure 12** shows the void area % as a function of local thickness strain for the three selected conditions. These results indicate that the extent of void formation increases with local thickness strain, consistent with data trends in other studies.[12,35] For all three conditions shown in Figure 12, the majority of voids were observed to nucleate at ferrite/martensite phase boundaries. Figure 12 shows that both 960TCR and 960AT conditions (hardness ratios of 2.3 and 2.7, respectively) exhibit lower void area % compared with the AR condition (hardness ratio = 3.2) for an equivalent local thickness strain, indicating that a lower hardness ratio suppressed microstructural damage. The lower void area % in response to the

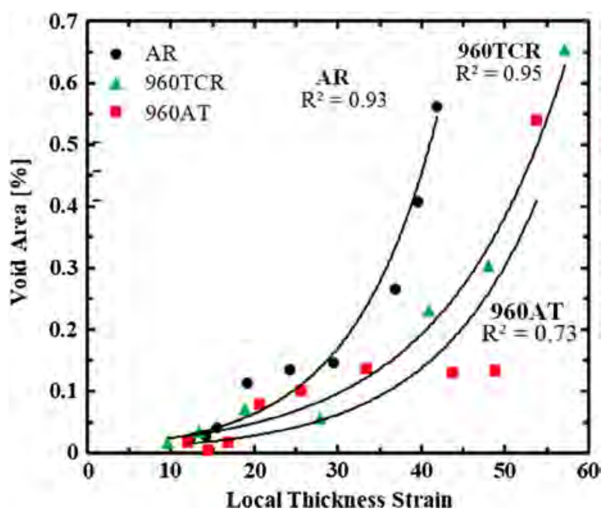

Figure 12. Void area % as a function of local thickness strain for the AR, 960AT, and 960TCR conditions.

lower hardness ratios for the 960AT and 960TCR conditions indicates that higher stresses and stress triaxiality are necessary to generate the critical population of voids to induce fracture. One index of stress triaxiality is the maximum thickness strain at tensile fracture: 42.5% for the AR condition; 58.9% for the 960AT condition; and 63.5% for the 960TCR condition using Equation (2). The observation of the higher maximum thickness strains in the 960TCR and 960AT samples is consistent with the interpretation that void formation in materials with low hardness ratios requires higher imposed strains to develop the critical local strain gradients that cause void nucleation and growth. The reduction in martensite hardness via tempering for the 960AT and 960TCR conditions was the primary reason leading to the increase in the local critical strains for void formation, which is consistent with the results based on a tomographic X-ray analysis study of Pushkareva *et al.* that concluded that tempering reduced the rate of void formation with strain in a DP steel by approximately a factor of four.[45]

4. Discussion

Figure 7a shows that HER increased with a decrease in hardness ratio and the results associated with Figure 12 indicated that the maximum thickness strain at ductile failure in a tensile test increased with a decrease in hardness ratio. Therefore, it can be hypothesized that an increase in HER should correlate with an increase in maximum thickness strain in tension.[10,66,67] The maximum thickness strains for the AR, 960AT, and 960TCR conditions were converted to true fracture strain using Equation (3), where t_i and t_f are the initial and final thicknesses of the fractured tensile specimen, and w_i and w_f are the initial and final widths.

$$\text{True Fracture Strain}\,(\varepsilon_f) = \ln\left[\frac{(t_i \times w_i)}{(t_f \times w_f)}\right] \tag{3}$$

Figure 13 compares HER versus true fracture strain data from two previous studies with data for the AR, 960AT, and 960TCR conditions (open squares).[10,67] In Figure 13, the data from Link and Chen, obtained on six different steels identified in the table inset, were representative of several different microstructural classes with UTS values ranging from approximately 450 to 860 MPa.[10] These data were considered as a single set exhibiting a linear fit with a high correlation coefficient (solid line, $R^2 = 0.98$). Data from Pushkareva *et al.* obtained on a single 0.15 wt% C steel intercritically annealed and quenched to produce multiple MVF conditions (approximately 62% or greater than 86%) showed similar trends, but with differing slopes.[67] The authors interpreted their data with linear fits and showed that the results correlated as two distinct groups depending on MVF. The resulting published trend lines for the two groups (MVF = 62%, and MVF > 86%) are included as dashed lines in Figure 13 without data points for clarity and show results distinctively different from the results of Link and Chen, suggesting that there is at least an MVF dependence to HER versus true fracture strain correlations. The data obtained for the AR, 960AT, and 960TCR conditions are consistent with the results of Link and Chen, indicating that true fracture strain in a tensile sample might be used as a reasonable measure of HER.[10] However, the

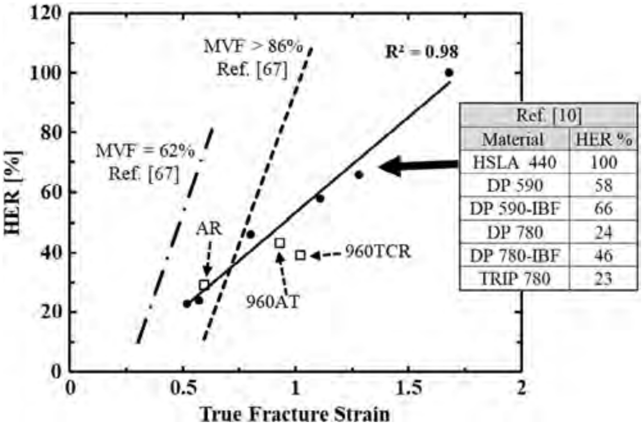

Figure 13. True fracture strain observed in tensile testing correlated to HER for three datasets originating from three distinctively different studies. The datasets from Link and Chen (solid line, solid circles) include results from six steel alloys with tensile strengths from 450 to 860 MPa.[10] The trend lines from Pushkareva et al. (dashed lines) summarize data obtained on a single 0.15 wt% C steel intercritically annealed and quenched to obtain high MVF amounts.[67] Results for the AR, 960AT, and 960TCR steels are shown by the identified open squares.

HER versus true fracture strain correlations from three distinctively different studies shown in Figure 13 indicate a complex relationship not definable by a single "master" function.

In addition to the correlations of HER with constituent properties (Figure 7a and 8), correlations of HER with tensile properties were also considered because past studies have shown reasonable success at accurately predicting HER values using tensile properties for select groups of steels.[19,20,68] **Figure 14**a correlates HER with uniform strain (UE) and Figure 14b correlates HER with YS/UTS ratio for the AR and eight modified conditions. For both AT and TCR datasets, an increase in HER corresponds to a decrease in UE and an increase in YS/UTS ratio. Tensile properties in Figure 14 were selected as both are often used as measures of formability, i.e., an increase in UE indicates an increase in ductility, and a decrease in YS/UTS ratio indicates an increase in the extent of work hardening, a parameter which is typically viewed as enhancing formability.

The inverse relationship between HER and UE in Figure 14a highlights and explains a unique and dichotomous characteristic of multiphase DP steels in that ferrite/martensite hardness characteristics which promote "local" formability (i.e., HER) differ from those that extend strain limits in either uniaxial or biaxial stretching (commonly referred to as "global" formability). A trend similar to Figure 14a was also observed in a study of a single alloy intercritically annealed and quenched to systematically vary MVF, where conditions with high MVF resulted in limited uniform strain but high HER values.[45] A potential reason for the difference in slopes between the AT and TCR conditions in Figure 14a is that the AT conditions exhibited YPE in amounts that increase with extent of tempering, which could account for a portion of the increased UE and corresponding lower UTS values, which have been shown to be coupled in a previous analysis of strain hardening in DP steels.[69] While the observation in Figure 14b that an increase in YS/UTS (i.e. decrease in extent

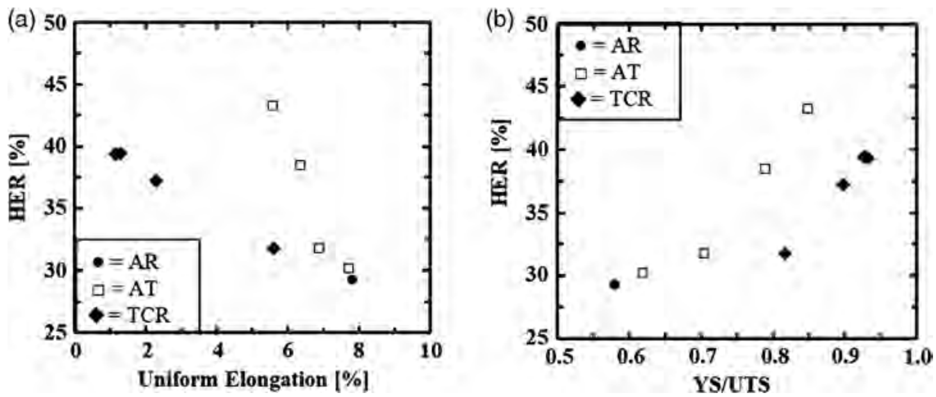

Figure 14. Correlations of HER with tensile properties for the AR and eight modified conditions: a) HER versus UE, and b) HER versus the ratio of yield to tensile strength (YS/UTS).

of work hardening) leads to an increase in HER is consistent with past studies, the fact that the AT and TCR conditions exhibit different functional dependences not present in the correlation in Figure 8 further illustrates the importance of understanding constituent properties when evaluating processing variables that affect local formability in DP steels.[70] The data comparisons generated using the AR and eight modified conditions in this study with datasets in literature suggest that reductions in martensite/ferrite hardness ratios lead to increased local formability.[10,17,18,25,40,45,50,67] However, the observed differences between critical parameter correlations also reveal the interactive complexity of the microstructural properties that govern local formability, and indicate that additional research is necessary to gain the appropriate insight to allow the development of accurate models that incorporate the multiple different microstructural approaches that have been used to produce DP steels with enhanced local formability.

5. Conclusions

A commercially produced DP steel with 1081 MPa UTS was processed to create eight additional conditions by tempering and cold-rolling, processes shown to primarily affect constituent hardness properties. The isolated effects of constituent hardness on subsequent formability performance for higher-strength DP steels were evaluated using tensile and hole expansion testing. A lower martensite/ferrite hardness ratio (increased similarity between ferrite and martensite hardness) was interpreted to improve strain-sharing, which suppressed plastic strain localization leading to higher YS values and to higher fracture limits for HER.

Strain maps generated using DIC for the AR and 960TCR conditions at different stages of strain illustrate that, regardless of martensite/ferrite hardness ratio, strains heterogeneously develop in the microstructure at locations consistent with preferential void nucleation sites in DP steels. The hardness ratio primarily affected the magnitude of local strain at a given stress, with higher martensite/ferrite hardness ratios exhibiting larger local strain gradients. Strain was observed to preferentially localize inside ferrite grains, and the highest strains occurred in ferrite with close proximity to martensite. Upon further deformation, isolated regions of strain link to form bands of strain localization within the microstructure.

Void area % as a function of thickness strain in fractured ASTM E8 standard size tensile specimens showed a lower void area % at equivalent strains for the DP steels with lower hardness ratios, confirming that lower hardness ratios suppress microstructural damage. Larger maximum thickness strains were observed for the DP steels with lower hardness ratios, indicating that a higher stresses and stress triaxiality are required to produce the critical void condition for fracture. A larger maximum true thickness strain measured on fractured E8 tensile specimens corresponded to larger HER values, and the trend was consistent with results reported in the literature.

Acknowledgements

The authors gratefully acknowledge the support of the sponsors of the Advanced Steel Processing and Products Research Center, an industry/university cooperative research center at the Colorado School of Mines. The authors also acknowledge the support of Dr. Narayan Pottore of ArcelorMittal for providing the commercially produced DP steel and for providing one author (M.D.T.) access to their research facility for the lab rolling of the HER samples and the HER tests.

Conflict of Interest

The authors declare no conflict of interest.

Data Availability Statement

Research data are not shared.

Keywords

advanced high strength steels, digital image correlation, formability, hole expansion ratios, nanoindentation, strain partitioning, void damage

Received: May 14, 2021
Revised: June 27, 2021
Published online:

[1] R. G. Davies, *Metall. Trans. A* **1978**, *9*, 671.
[2] O. J. Kwon, K. Y. Lee, G. S. Kim, K. G. Chin, *Mater. Sci. Forum* **2010**, *638*, 136.
[3] R. Kuziak, R. Kawalla, S. Waengler, *Arch. Civil Mech. Eng.* **2008**, *9*, 2.
[4] D. Bhattacharya, N. Pottore, N. Fonstein, I. Gupta, in *Int. Conf. on Advanced High Strength Sheet Steels for Automotive Applications, Proceedings* (Eds.:J. G. Speer), AIST, Warrendale, PA **2004**, p. 119.
[5] K. Choi, A. Soulami, D. Li, X. Sun, M. Khaleel, L. Xu, F. Barlat, *SAE Int.* **2012**, *1*, 0042.
[6] M. Miura, M. Nakaya, Y. Mukai, *Kobelco Tech. Rev.* **2008**, *28*, 8.
[7] G. Rosenberg, I. Sinaiová, Ľ. Juhar, *Mater. Sci. Eng., A* **2013**, *582*, 347.
[8] J. H. Kim, M. G. Lee, D. Kim, D. K. Matlock, R. H. Wagoner, *Mater. Sci. Eng., A* **2010**, *527*, 7353.
[9] F. Hisker, R. Thiessen, T. Heller, *Mater. Sci. Forum* **2012**, *706*, 925.
[10] T. M. Link, G. Chen, in *Proc., Int. Symp. on New Developments in Advanced High-Strength Sheet Steels* (Eds.: E. De Moor, H. J. Jun, J.G. Speer, M. Merwin), AIST, Warrendale, PA **2013**, p. 63.
[11] C. Landron, E. Maire, O. Bouaziz, J. Adrien, L. Lecarme, A. Bareggi, *Acta Mater.* **2011**, *59*, 20.
[12] C. Landron, O. Bouaziz, E. Maire, J. Adrien, *Scr. Mater.* **2010**, *63*, 10.
[13] J. Dykeman, in *Proc., Int. Symp. on New Developments in Advanced High-Strength Sheet Steels* (Ed.: E. De Moor, H. J. Jun, J. G. Speer, M. Merwin), AIST, Warrendale, PA **2013**, p. 15.
[14] M. S. Walp, A. Wurm, J. F. Siekirk, A. K. Desai, *SAE Int.* **2006**, *1*, 1433.
[15] J. H. Kim, J. H. Sung, K. Piao, R. H. Wagoner, *Int. J. Plasticity* **2011**, *27*, 10.
[16] R. D. K. Misra, S. W. Thompson, T. A. Hylton, A. J. Boucek, *Metal. Mater. Trans. A* **2001**, *32*, 745.
[17] K. Hasegawa, K. Kawamura, T. Urabe, Y. Hosoya, *ISIJ Int.* **2004**, *44*, 3.
[18] M. D. Taylor, K. S. Choi, X. Sun, D. K. Matlock, C. E. Packard, L. Xu, F. Barlat, *Mater. Sci. Eng.,: A* **2014**, *597*, 431.
[19] R. J. Comstock, D. K. Scherrer, R. D. Adamczyk, *J. Mater. Eng. Perform.* **2006**, *15*, 6.
[20] S. K. Paul, *J. Mater. Eng. Perform.* **2014**, *23*, 10.
[21] N. Saeidi, A. Ekrami, *Mater. Sci. Eng., A* **2009**, *523*, 1.
[22] Z. Yu, R. Barabash, O. Barabash, W. Liu, Z. Feng, *Journal of Materials* **2012**, *65*, 21.
[23] J. Lee, S.-J. Lee, B. C. De Cooman, *Mater. Sci. Eng., A* **2012**, *536*, 231.
[24] K. Mori, Y. Abe, Y. Suzui, *J. Mater. Process. Technol.* **2010**, *210*, 4.
[25] C. P. Scott, B. S. Amirkhiz, I. Pushkareva, F. Fazeli, S. Y. P. Allain, H. Azizi, *Acta Mater.* **2018**, *159*, 112.
[26] M. J. Gibbs, Master Thesis, Colorado School of Mines, Colden, CO, USA **2011**.
[27] J. Kadkhodapour, A. Butz, S. Ziaei Rad, *Acta Mater.* **2011**, *59*, 7.
[28] K. Takashima, Y. Toji, K. Hasegawa, *Proc. Mater. Sci.* **2013**, 201.
[29] K. Alharbi, H. Ghadbeigi, P. Efthymiadis, M. Zanganeh, S. Celotto, R. Dashwood, C. Pinna, *Modell. Simul. Mater. Sci. Eng.* **2015**, *23*, 8.
[30] S. K. Paul, *Modell. Simul. Mater. Sci. Eng.* **2013**, *21*, 26.
[31] O. R. Jardim, W. P. Longo, K. K. Chawla, *Metallography* **1984**, *172*, 123.
[32] H. Ghadbeigi, C. Pinna, S. Celotto, J. R. Yates, *Mater. Sci. Eng., A* **2010**, *527*, 18.
[33] R. Petrov, L. Kestens, A. Wasilkowska, Y. Houbaert, *Mater. Sci. Eng., A* **2007**, *447*, 1.
[34] M. D. Taylor, PhD Thesis, Colorado School of Mines, Golden, CO, USA **2016**.
[35] D. L. Steinbrunner, D. K. Matlock, G. Krauss, *Metall. Trans. A* **1988**, *19*, 579.
[36] E. Maire, O. Bouaziz, M. Di Michiel, C. Verdu, *Acta Mater.* **2008**, *56*, 18.
[37] C. Landron, O. Bouaziz, E. Maire, J. Adrien, *Acta Mater.* **2013**, *61*, 6821.
[38] G. Avramovic-Cingara, Y. Ososkov, M. K. Jain, D. S. Wilkinson, *Mater. Sci. Eng., A* **2009**, *516*, 1.
[39] C. C. Tasan, J. P. M. Hoefnagels, M. G. D. Geers, *Scr. Mater.* **2010**, *62*, 11.
[40] J. Kang, Y. Ososkov, J. D. Embury, D. S. Wilkinson, *Scr. Mater.* **2007**, *56*, 11.
[41] X. Sun, K. S. Choi, A. Soulami, W. N. Liu, M. A. Khaleel, *Mater. Sci. Eng.., A* **2009**, *526*, 1.
[42] N. Saeidi, F. Ashrafizadeh, B. Niroumand, F. Barlat, *J. Mater. Eng. Perform.* **2014**, *24*, 1.
[43] S. Sagadopan, N. Ramisetti, H. Yao, **2010**, https://www.researchgate.net/publication/289351200_Influence_of_microstructural_attributes_on_formability_of_cold_rolled_DP980_sheet_steels (accessed: November 2015)
[44] C. Nikhare, P. D. Hodgson, M. Weiss, *Mater. Sci. Eng., A* **2011**, *528*, 6.
[45] I. Pushkareva, C. P. Scott, M. Gouné, N. Valle, A. Redjaïmia, A. Moulin, *ISIJ Intl.* **2013**, *53*, 7.
[46] S. K. Basantia, P. K. Prusty, D. Das, N. Khutia, *Mater. Today: Proc.* **2020**, *33*, 5055.
[47] R. Gou, W. Dan, W. Zhang, M. Yu, *Mater. Res. Express* **2017**, *4*, 7.
[48] A. H. Jahanara, Y. Mazaheri, M. Sheikhi, *Mater. Sci. Eng., A* **2019**, *764*, 138206.
[49] R. Rodriguez, I. Gutierrez, *Mater. Sci. Eng., A* **2003**, *361*, 377.
[50] Y. Chang, M. Lin, U. Hangen, S. Richter, C. Haase, W. Bleck, *Mater. Des.* **2021**, *203*, 109620.
[51] A. N. Bortsov, N. M. Fonshteyn, *Phys. Met. Metall.* **1986**, *61*, 2.
[52] G. Krauss, *Steels*, ASM International, Materials Park, OH **2005**.
[53] A. Anazadeh Sayed, S. Kheirandish, *Mater. Sci. Eng., A* **2012**, *532*, 21.
[54] R. L. Higginson, C. M. Sellars, *Worked Examples in Quantitative Metallography*, Maney Publishing, University of Virginia, London **2003**.
[55] Q. Furnemont, M. Kempf, P. J. Jacques, M. Goken, *Mater. Sci. Eng., A* **2002**, *328*, 26.
[56] A. C. Fischer-Cripps, *Surf. Coat. Technol.* **2006**, *200*, 4153.
[57] W. C. Oliver, G. M. Pharr, *J. Mater. Res.* **1992**, *7*, 6.
[58] M. D. Taylor, Master Thesis, Colorado School of Mines, Golden, CO, USA **2013**.
[59] F. Lagattu, F. Bridier, P. Villechaise, J. Brillaud, *Mater. Charact.* **2006**, *56*, 1.
[60] J. Blaber, 2D digital image correlation MATLAB program, http://www.ncorr.com/ (accessed: May 2021).
[61] M. S. Rashid, B. V. N. Rao, *Metall. Trans. A* **1982**, *13*, 10.
[62] G. R. Speich, A. J. Schwoeble, G. P. Huffman, *Metall. Trans. A* **1983**, *14*, 6.
[63] J. Moon, S. Kim, J. Jang, J. Lee, C. Lee, *Mater. Sci. Eng., A* **2008**, *487*, 1.
[64] T. Ohmura, K. Tsuzaki, *J. Mater. Sci.* **2007**, *42*, 5.
[65] K. Hayashi, K. Miyata, F. Katsuki, T. Ishimoto, T. Nakano, *J. Alloys Compd.* **2013**, *577*, S593.
[66] O. R. Terrazas, K. O. Findley, C. J. Van Tyne, *ISIJ Int.* **2017**, *57*, 937.
[67] I. Pushkareva, S. Allain, C. P. Scott, A. Redjaïmia, A. Moulin, *ISIJ Int.* **2015**, *55*, 2237.
[68] B. S. Levy, C. J. Van Tyne, *Journal of Materials Engineering and Performance* **2012**, *21*, 2147.
[69] D. K. Matlock, G. Krauss, F. Zia–Ebrahimi, *Deform. Process. Struct. ASM* **1983**, *2*, 47.
[70] S. B. Lee, PhD Thesis, Colorado School of Mines, Golden, CO USA **2005**.